Noise Levels and Signals Observed on Submarine Fibers in the Canary Islands Using DAS

Arantza Ugalde*[1], Carlos Becerril[2], Antonio Villaseñor[1], César R. Ranero[1,3], María R. Fernández-Ruiz[2], Sonia Martin-Lopez[2], Miguel González-Herráez[2], and Hugo F. Martins[4]

Abstract

In this study, we investigate 70 days of distributed acoustic sensing (DAS) recordings in the Canary Islands using an undersea fiber-optic telecommunication cable that links the islands of Tenerife and Gran Canaria. Two DAS interrogators connected to both ends of the cable turned the fiber into an array of 11,968 strain sensors covering a total length of ∼120 km. We present the details of the experiment, noise analysis, and examples of recorded signals. Seismic ambient noise levels assessment indicates poor local coupling of the cable due to the irregular bathymetry that results in high-amplitude acoustic oscillations in some channels. The DAS array recorded several types of nonseismic (vehicles, surface gravity waves, ships) and seismic signals. Local and regional earthquakes were detected with magnitudes $m_{bLg} \geq 2$. Surface waves from teleseismic events at a distance of ∼3000 km were also identified in the strain recordings. Here, we report the first observations with DAS of hydroacoustic *T* waves generated by oceanic earthquakes located at the Central Mid-Atlantic Ridge and the Cape St. Vincent region. Events had magnitudes from M_w 4.2 to 6.9, and the hydroacoustic waves were recorded at epicentral distances from 780 to 3400 km. Our findings show that submarine fiber-optic cables can effectively be used to assess the seismic activity in remote oceanic areas.

Cite this article as Ugalde, A., C. Becerril, A. Villaseñor, C. R. Ranero, M. R. Fernández-Ruiz, S. Martin-Lopez, M. González-Herráez, and H. F. Martins (2021). Noise Levels and Signals Observed on Submarine Fibers in the Canary Islands Using DAS, *Seismol. Res. Lett.* **93**, 351–363, doi: 10.1785/0220210049.

Supplemental Material

Introduction

From 21 July to 1 October 2020, we carried out an undersea experiment to monitor the seismicity in the Canary Islands using fiber-optic distributed acoustic sensing (DAS). This technology has the ability of turning a kilometer-length fiber-optic cable into a very dense array of synchronized strainmeters oriented along the fiber. Effectively, an independent strain-rate measurement is obtained every few meters along the fiber. It is an emerging technology with strong potential for seismic monitoring (see Zhan, 2020; Lindsey and Martin, 2021). Fiber-optic seismology gained popularity in the oil and gas industry a decade ago, but interest in it is growing rapidly in a variety of geophysical applications. Some of them include active-source hydroacoustic monitoring in the ocean (Matsumoto *et al.*, 2021), CO_2 storage monitoring (Trautz *et al.*, 2020), imaging of marine sediments (Spica *et al.*, 2020), urban seismology (Lindsey *et al.*, 2020; Zhu *et al.*, 2021), seismic properties of glaciers (Booth *et al.*, 2020), teleseismic studies (Yu *et al.*, 2019), characterization of thunder-induced ground motions (Zhu and Stensrud, 2019), active-source seismic tomography (Parker *et al.*, 2018), and ambient noise interferometry and earthquake seismology (Ajo-Franklin *et al.*, 2019).

Previous studies using DAS on subsea fibers (Lindsey *et al.*, 2019; Sladen *et al.*, 2019; Williams *et al.*, 2019) have revealed a variety of seismic signals with frequencies ranging from mHz to Hz on the strain recordings and consistency with the response of nearby broadband seismometers, thus strengthening the potential of this technology for marine seismology. However, the quality of the recordings is dependent on the cable coupling to the seafloor (e.g., Lior *et al.*, 2021) and on the cable sensitivity related to its internal structure. In this study, we took advantage of one of the existing submarine telecommunication cables that are deployed between the islands of Tenerife (TF) and Gran Canaria (GC). Two DAS interrogator units were connected to both landing ends of the fiber continuously recording the seismic wavefield. The submarine cable, owned by CANALINK-

1. Institute of Marine Sciences, ICM-CSIC, Barcelona, Spain, https://orcid.org/0000-0001-8592-4832 (AV); 2. Department of Electronics, University of Alcalá, Alcalá de Henares, Spain, https://orcid.org/0000-0002-7831-6940 (CB); https://orcid.org/0000-0003-3561-2405 (MRF-R); 3. Institució Catalana de Recerca i Estudis Avançats, ICREA, Barcelona, Spain; 4. Instituto de Óptica, CSIC, Madrid, Spain, https://orcid.org/0000-0003-3927-8125 (HFM)

*Corresponding author: a.ugalde@icm.csic.es

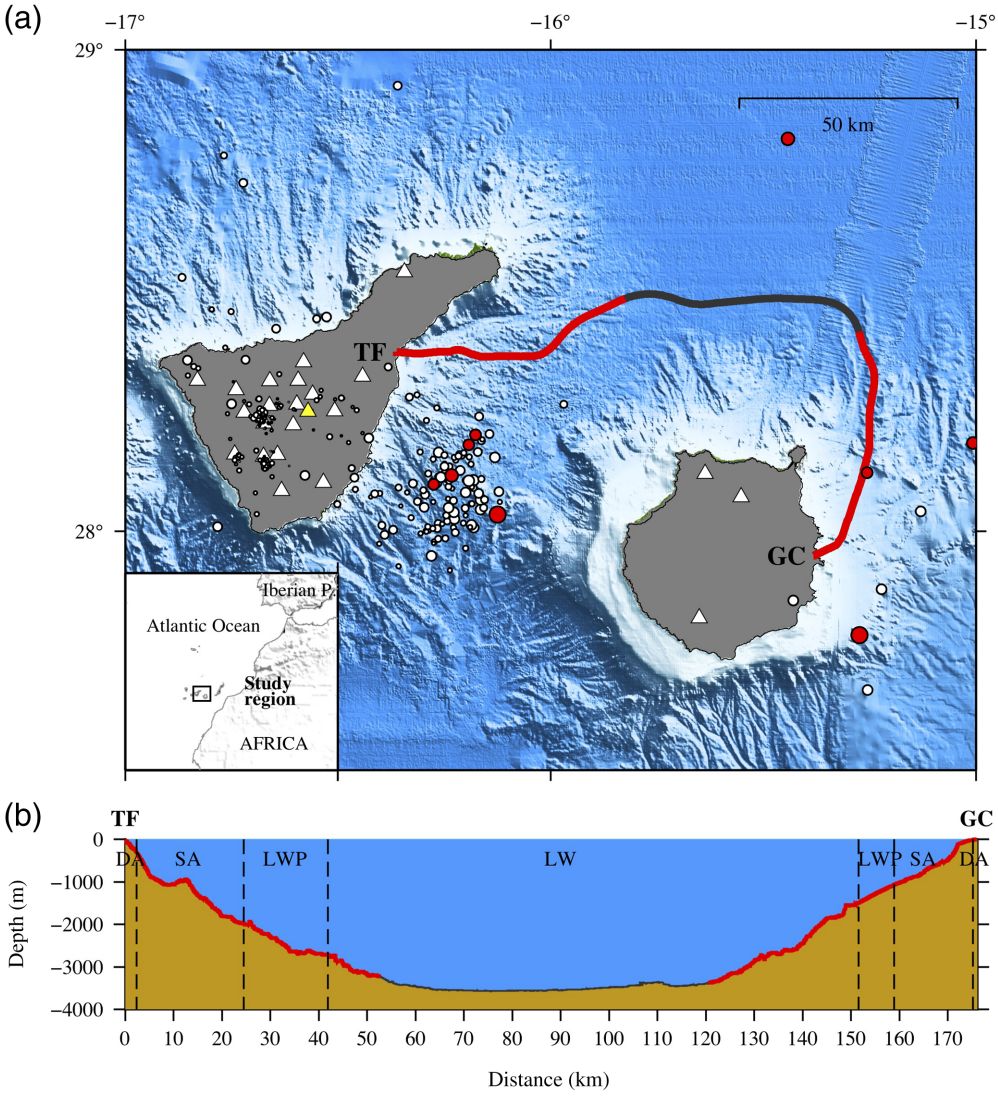

Figure 1. (a) Location map of the telecommunication fiber-optic cable between the islands of Tenerife (TF) and Gran Canaria (GC). Two distributed acoustic sensing (DAS) interrogators acquired data along ~60 km segments (red lines) of the total ~176-km-long cable (dark line). Seismicity occurred in the study region from July to September 2020 according to the Instituto Geográfico Nacional (IGN) catalog (see Data and Resources) is plotted with solid circles. Earthquakes are scaled by magnitude in the range $-0.1 \le m_{bLg} \le 3.1$. Red circles mark the epicenters with magnitudes >2. Solid triangles indicate the location of the permanent seismic stations of the Spanish National Seismic Network. The yellow triangle plots the location of the land station MACI, in TF, used for waveform comparison. (b) Bathymetric profile along the fiber-optic cable route. Dashed vertical lines separate sections of lightweight (LW), lightweight-protected (LWP), single-armored (SA), and double-armored (DA) cable. For bathymetric data, see Data and Resources. The color version of this figure is available only in the electronic edition.

Canarias submarine link S.L., has a total length of ~176 km and lies over the seafloor, reaching a maximum depth of 3570 m below sea level (Fig. 1). We interpolated the fiber positions from the cable locations provided by CANALINK and extracted the corresponding bathymetric profile from the available bathymetry grid (see Data and Resources). The profile plotted in Figure 1 corresponds to the undersea section of the cable and does not include the on-land path from the shore to the interconnection center where the DAS interrogators were installed (~7 km in TF and ~4 km in GC). Thus, the DAS spatial axis has the origin ("0 m") set to the cable position at the shoreline.

In this work, we present the instrumentation used and explore the features of the signals recorded in different sections of the cable in the submarine environment of the Canary Islands. We also analyze the noise levels of the DAS recordings. Then we report a variety of observations of seismic and nonseismic sources recorded during a monitoring period of 70 days, including regional and teleseismic earthquakes and hydroacoustic signals from ships. We also show that the DAS technology is capable of recording, with high sensitivity, *T* waves from a number of submarine earthquakes in the Atlantic Ocean.

The Fiber-Optic Cable

The submarine cable used in this study is a 12-fiber, URC2 14 mm cable with a total length of ~176 km (G654, see Fig. S1, available in the supplemental material to this article). The specified maximum attenuation is 0.18 dB/km (at 1550 nm wavelength). The cable is largely composed of a single mechanical piece with no periodical junctions or optical splices that was laid on the ocean floor (i.e., not buried). The cable is passive, with no optical amplifiers or electrical power. Along the cable, the mechanical protection varies significantly, ranging from lightweight cable in deep water, lightweight protected cable, single armored cable, and double-armored cable at shallow depths close to the shoreline (Fig. 1b). Although the mechanical isolation or coupling of the fiber cores is not

specified, it is expected to vary significantly depending on the type of protection.

Instrumentation and Data Preprocessing

In this experiment, two chirped-pulse DAS (CP-DAS) interrogators (see Text S1 for the instrument technology background) monitored 5984 channels each (equivalent to 11,968 independent seismometers) with a spatial resolution (optical and gauge length) of 10 m in a single-ended configuration, that is, the first 60 km of fiber starting from the coastline and into the sea (Fig. 1). Raman amplification was used to mitigate the fiber losses (Pastor-Graells *et al.*, 2017) and flatten the instrumental performance along the fiber. We set the instrumental data acoustic sampling frequency to 1 kHz (imposed by the repetition rate of the train of pulses launched into the fiber and related to the fiber size). The recorded strain data were later downsampled to 50 Hz, determined to be enough to accurately depict the seismic phenomena of interest, and to reduce the dataset size. To isolate the acoustic band of interest, we applied a band-pass filter between 0.05 and 24 Hz to the data in postprocessing.

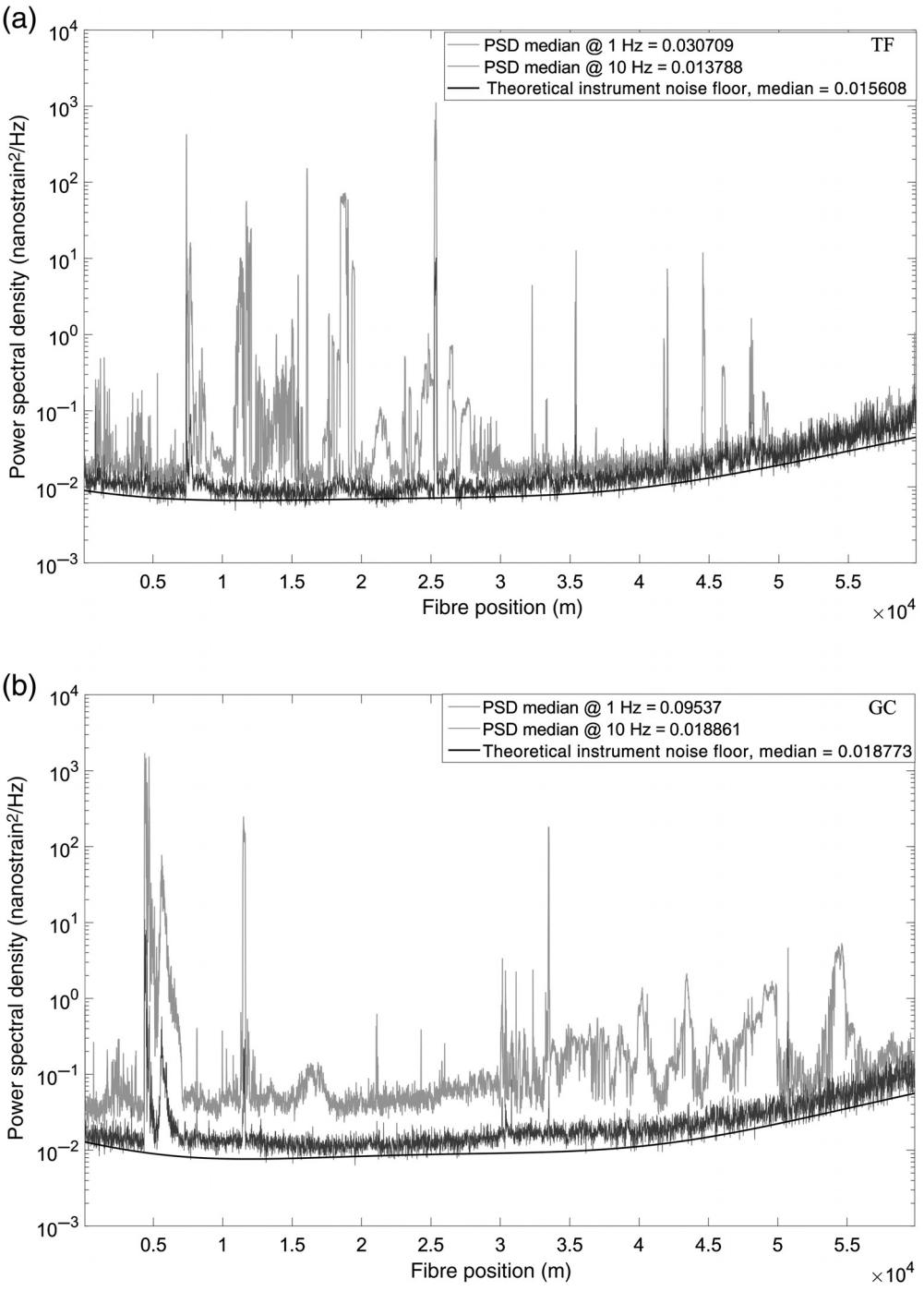

Figure 2. Power spectral density (PSD) of the recorded acoustic signal at 1 and 10 Hz compared with the estimated instrumental noise along the 60-km-length fiber. Interrogated in (a) TF and (b) GC. For each spatial point along the fiber, the PSD is computed using a time window of 1 hr, recorded at 3 a.m. to minimize the anthropogenic noise. The Cramér–Rao lower bound (CRLB) gives the theoretical instrumental acoustic noise floor. This can be computed from the optical power profile recorded along the fiber (Costa *et al.*, 2019).

Noise Levels

For frequencies above a few Hertz, the acoustic noise floor was largely set by instrumental noise along the fiber (see the power spectral density [PSD] at 10 Hz vs. instrumental noise in Fig. 2), with the exception of a few persistent sections, with high-noise peaks related to environmental noise. The instrumental PSD noise floor varies less than 10 dB (between 0.01 and 0.1 $n\varepsilon^2/Hz$) over the span of 60 km. This is the maximum range of the CP-DAS at the sampling frequency of 50 Hz.

A visual inspection of the continuous raw strain data from the fiber array along the 70-day recording period finds a low

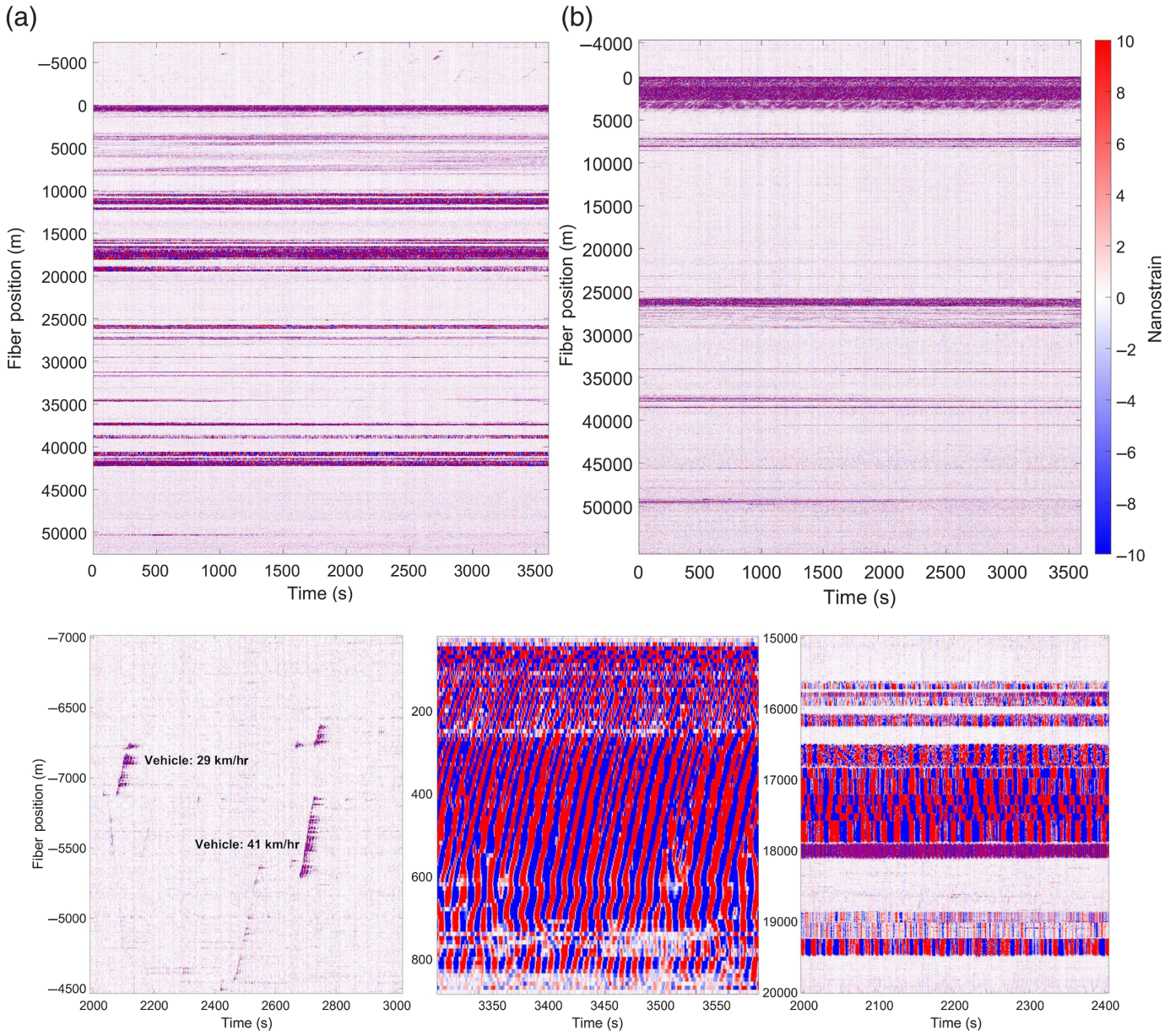

signal-to-noise ratio (SNR) at some channels, whereas others have a high SNR, especially in TF (see Fig. 3), a behavior that remained throughout the duration of the experiment. At frequencies <1 Hz (see Fig. 2), the acoustic noise alternated between instrumental noise and ambient noise along the cable, varying by several orders of magnitude from point to point. Furthermore, several sections in which lower ambient acoustic noise was systematically registered correlated with the sections in which the seismic events were detected with lower amplitudes. This appears to indicate that the mechanical strain coupling between the cable and the ground (and possibly local ambient noise) is highly variable along the cable.

To assess quantitatively the typical seismic ambient noise levels, we analyzed the data spectral characteristics of several channels of the array by computing the PSD over a 12-hr-length time segment at 22-min-long, 50% overlapped intervals,

Figure 3. About 1 hr of DAS array recordings at 3 a.m. (time domain, in units of nanostrain) showing alternating noisy and quiet fiber positions at (a) TF and (b) GC arrays. Fiber position origin (0 km) is relative to the shoreline, and negative values correspond to the on-land fiber segment leading to the interconnection center where the DAS interrogators were installed. The insets in the bottom are a zoom-in on strain recordings from sections of the DAS array showing on-land vehicle traffic, along with their estimated speed (left); surface gravity waves propagating at shallow depths (center); uneven cable strain coupling conditions, with sharp transitions between noisy and quiet sections and with different local resonating frequencies in neighboring points (right). The color version of this figure is available only in the electronic edition.

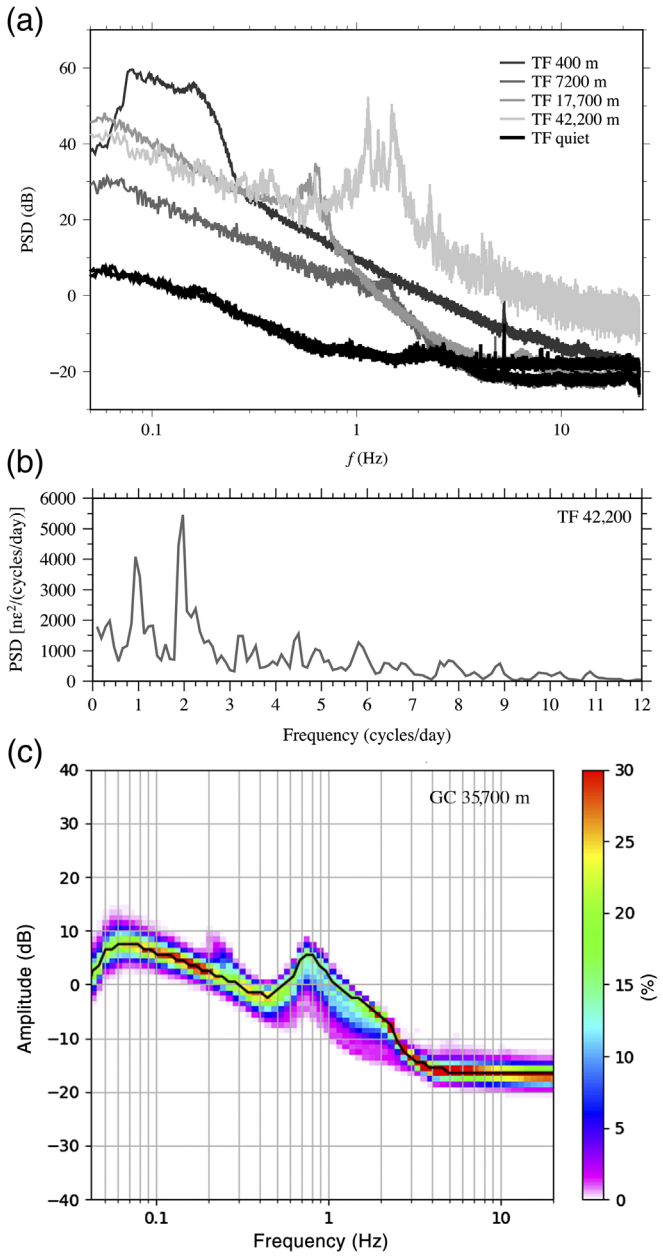

Figure 4. (a) PSD (in dB related to $n\varepsilon^2$/Hz) for 12 hr of noise recordings at TF. The noise levels at fiber locations 400 m, 7200 m, 17,700 m, 42,200 m, and two quiet channels (−6300 and 37,700 m) are plotted. (b) PSD of the 1–2 Hz band-pass-filtered root-mean-square (rms) strain amplitude for 22 days of recordings at position 42,200 m. Diurnal (1 cycle/day) and semidiurnal (2 cycles/day) periods are dominant. (c) Probability density function (PDF) at position 35,700 m of GC array constructed using 9900 PSD during the period from July to September 2020. The black line plots the mode. The color version of this figure is available only in the electronic edition.

on a quiet day. As an example, Figure 4a shows the median power spectra for four noisy channels (0.4, 7.2, 17.7, and 42.2 km) and two relatively quiet locations (−6.3 km onshore and 37.7 km offshore) on the TF array. It can be observed that the PSDs at the two quietest locations almost overlap in the frequency band 0.05–24 Hz, being essentially set by instrumental noise. Noise levels at 7.2 and 17.7 km are also comparable to the quiet channels for frequencies >2 Hz. In general, the noisy channels show high amplitudes for frequencies <2 Hz. The primary (frequencies <0.1 Hz) and secondary (frequencies in the 0.1–1 Hz range) microseisms are not visible in the PSDs, even in the quietest channels. A pronounced noise peak is observed at 0.4 km, at ∼24-m-water depth, in the 0.07–0.2 frequency band. These oscillations are caused by surface gravity waves that affect the strain recordings at shallow depths (<∼100 m; e.g., Sladen *et al.*, 2019). A marked noise peak is also noticeable at 42.2 km, at a water depth of ∼2800 m, for frequencies between 1 and 2 Hz. To investigate the spectral characteristics of this noise peak, we computed the root mean square (rms) strain amplitudes using 1-hr-long, 50% overlapped windows for 22 days of continuous data filtered in the 1–2 Hz frequency band. Autospectral analysis shows dominant diurnal (1 cycle/day) and semidiurnal (2 cycles/day) periodicities, which support a tidal modulation of the dominant strain amplitudes in this location (Fig. 4b). We also computed the probability density function according to McNamara and Buland (2004) for the entire dataset recorded at a quiet position (35,700 m and ∼2500-m-water depth) of GC array. The primary and secondary microseisms can be observed (Fig. 4c).

Observations

In the following, we report the detection of a variety of signals in the 70-day recordings of the Canary Islands submarine DAS array.

Nonseismic signals (ships)

Ocean-bottom seismometers (OBSs) and hydrophone arrays commonly record seismic and hydroacoustic signals from ships. These signals have been used, for instance, as a source of opportunity for locating and orienting ocean-bottom instrumentation (e.g., Trabattoni *et al.*, 2020). Because of its geostrategic location, the Canary archipelago presents intensive ship traffic. Ugalde *et al.* (2019) already reported a large number of ship signatures on OBS and hydrophone recordings at depths between 709 and 1355 m in this region. Rønnekleiv *et al.* (2019) showed that DAS is capable of recording acoustic waves from ships, too. Rivet *et al.* (2021) further explored the potential of this technology to detect and track ships. They concluded that the strain changes in the cable can be caused directly by pressure waves traveling through the water layer or through the sediments for slightly buried sections of the cable. In our experiment, the DAS arrays recorded maritime traffic with high SNR. Figure 5 shows an example of a vessel recorded at GC (fiber position 11,020 m, ∼760-m-water depth). The spectrogram shows the typical pattern and tonals of ship-radiated acoustic signals. The ship's signature, which is

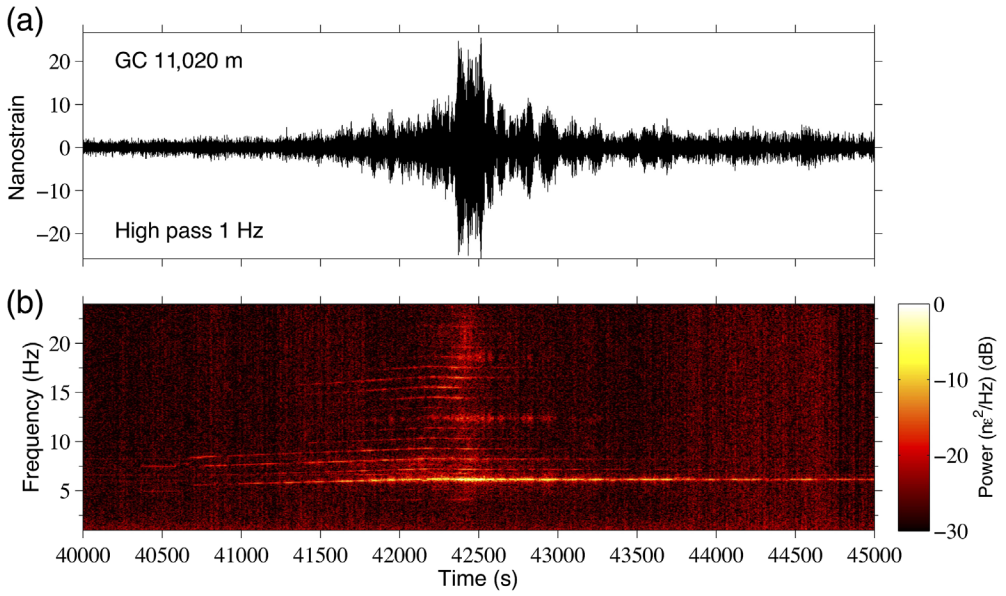

Figure 5. (a) Strain observations (in units of nanostrain) and (b) spectrogram at GC array of a vessel (fiber position 11 km, time in seconds from 9 August 2020 00:00:00). The color version of this figure is available only in the electronic edition.

mainly related to the characteristics of the engine and propeller rotation, can be observed for more than one hour. Doppler spectral gliding, generated by the relative motion between the source and the receiver, is clearly observed as the ship approaches the fiber. At the closest point of approach, narrow spectral lines span from ~6 to 24 Hz (the maximum frequency that could be investigated). A diesel generator aboard the ship, which commonly has rotation speeds of 720 rpm, causes the acoustic noise peak at 6 Hz. These observations confirm the capability of DAS for monitoring ocean vessels. This technology has also potential as a future preventive technology for submarine cable protection from human hazards (trawlers, anchor hits), a field in which a very limited experimental work has been performed to date (Rønnekleiv *et al.*, 2019).

Local and regional earthquakes

The Canary Islands are an active volcanic archipelago that presents moderate seismicity. A fault system located between the islands of TF and GC is the most seismically active structure in the region (Fig. 1) and was the source of the largest instrumentally recorded earthquake in the archipelago (*M* 5.2; Mezcua *et al.*, 1992). The Instituto Geográfico Nacional (IGN, network code ES) operates the permanent, land-based, seismic network in the Canary Islands. Since the first seismic station was installed in TF in 1964, the network in the archipelago has been improved over the years and is now composed of 48 seismic stations, of which there are 20 in TF and three in GC. However, despite the significant increase in instrumentation, locations of earthquakes in offshore areas are still poorly constrained, particularly in depth, because of the lack of nearby stations. Therefore, the availability of DAS data through submarine cables could provide very valuable constraints for earthquake location.

We tried, initially, an approach used in traditional seismology to detect seismic signals. Taking into account the noise level observations, we used a triggering algorithm based on short-term average (STA)/long-term average (LTA) (FilterPicker; Lomax *et al.*, 2012) on low-noise fiber locations. However, the algorithm only was able to detect the strongest events of the IGN catalog in this region. Therefore, an analyst visually inspected the data using two approaches: (1) examining the whole dataset and spectrograms of some individual low-noise channels and (2) looking at all the traces using the time segments of the events reported in the IGN catalog. For the period of time, the experiment was in progress, the IGN land seismic network located a total of 125 earthquakes offshore TF and GC, with m_{bLg} magnitudes ranging from 0.6 to 3.1. Among them, the nine events of the catalog having magnitudes $m_{bLg} \geq 2.1$ and three $m_{bLg} \geq 2.0$ events were confirmed visually by the analysis of the fiber data. They are plotted with red solid circles in Figure 1. The fiber array also recorded the strongest seismic event of the catalog during this period, a m_{bLg} 3.2 earthquake that occurred in the Atlantic at ~169 km north from the cable. Figure 6 shows an example of the raw DAS array recordings during the m_{bLg} 3.1 earthquake occurred in the fault between TF and GC at 34 km depth. The direct-wave arrivals of the earthquake signals are clearly observed as they propagate along the array. The change in the slope of the travel-time curves from ~35 km to the end of the fiber marks the change in the direction of the cable that can be observed in Figure 1. Figure 7 plots the strain recorded at a single fiber location compared with the recordings of a land station at about the same epicentral distance (MACI, equipped with a Streckeisen STS-1V/VBB seismometer, see the station location in Fig. 1). *P*, *S*, and coda waves can be clearly identified in both recordings. The spectrograms show that the earthquake is seen between 2 and 15 Hz in the DAS recordings, whereas the frequency content is higher in the land station. It can also be noted that *S*-wave coda amplitudes show lower

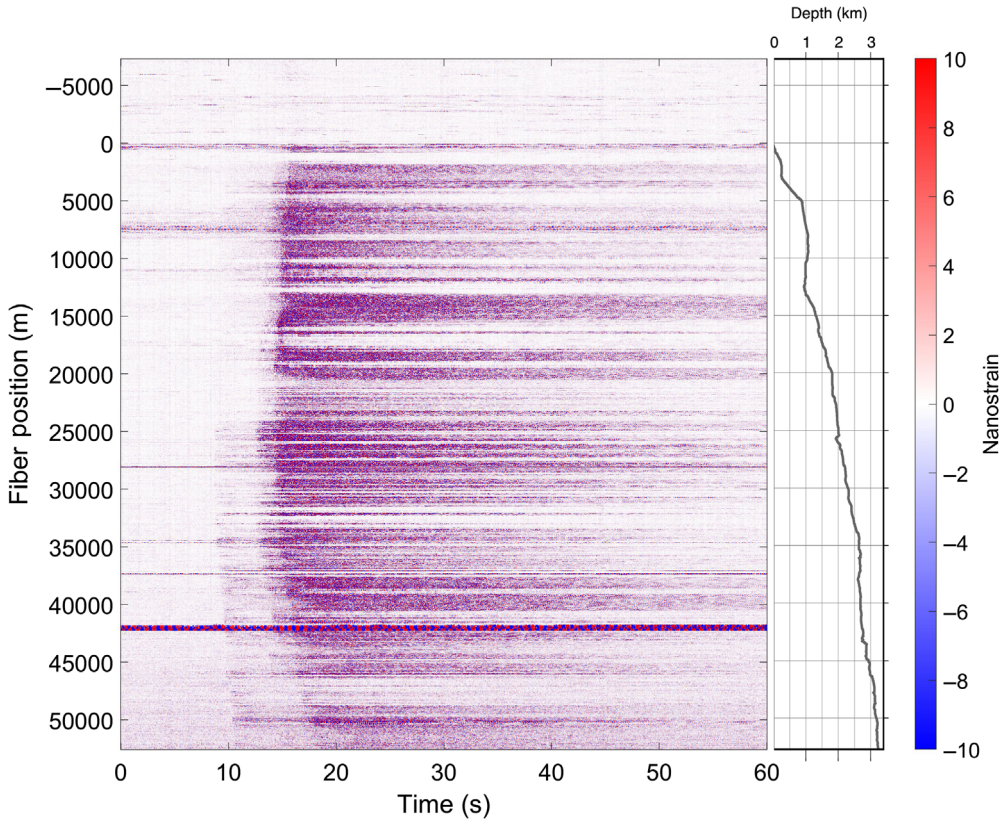

Figure 6. About 2 Hz high-pass-filtered DAS recordings (time domain, in units of nanostrain) of the 27 July 2020 m_{bLg} 3.1 earthquake for the 5984 locations of the TF array at 10 m spacing. Time is relative to the origin time of the earthquake. The channel depths are also plotted. Fiber position origin (0 km) is relative to the shoreline. The color version of this figure is available only in the electronic edition.

attenuation for the oceanic path (strain recordings at 37.7 km in ~2700-m-water depth) than for the island seismic station.

Teleseismic events

During the experiment, the DAS array also recorded teleseismic events. The largest one had a magnitude of M_w 6.9 and occurred in the Central Mid-Atlantic Ridge at 10 km depth, according to the U.S. Geological Survey (USGS). Figure 8d shows the DAS array teleseismic observations of this earthquake. The epicentral distance is 3281 km to the midpoint of the TF's segment of the array. Figure 8a–c shows, as a comparison, the recordings at MACI land seismic station. The main body-wave arrivals, which are clearly recorded at MACI, are close to the noise level in DAS, which is capable of recording the energy of surface waves, as shown in Figure 8d. The raw strain data show a strong late arrival at about 2200 s from the earthquake origin time that also appears at MACI when the seismogram is high-pass filtered at 1 Hz. This strong energy corresponds to hydroacoustic *T* waves and is examined in the Hydroacoustic Phases section.

Hydroacoustic phases

T waves (the label *T* for tertiary arrival) are seismically generated acoustic waves that propagate in the SOFAR (for SOund Fixing And Ranging) channel of minimum sound velocity through the oceans. They can be excited by earthquakes through the conversion of elastic energy into acoustic waves at the solid–liquid interface (e.g., Talandier and Okal, 1998; Park *et al.*, 2001). *T* waves recorded on seismograph and hydrophone networks have been used in a large number of investigations, including studies of small earthquake detection and retrieval of seismic source properties in marine environments (Okal and Talandier, 1986), detection of volcanic activity (Talandier and Okal, 1987), underwater landslides (Fryer *et al.*, 2004), and global climate change (Wu *et al.*, 2020). *T* phases are useful to locate seismicity at midoceanic ridges because, due to the low attenuation at the SOFAR channel, they can transmit energy from relatively small sources over large epicentral distances. By combining the *T*-wave amplitude and duration, they can be also used to estimate the source size and to discriminate the source type.

During this experiment, the DAS array recorded hydroacoustic *T* waves from several earthquakes, most of them located in the Central Mid-Atlantic Ridge at shallow depths (10 km) and magnitudes M_w 4.5–6.9 at distances from ~3100 to ~3400 km (USGS). We also identified *T* waves from a M_w 4.6 earthquake located in the Azores Islands region at a distance of ~1900 km (USGS). The closest event that generated *T* waves and was detected by the DAS arrays occurred in Cape St. Vincent region at 780 km distance and had a magnitude M_w 4.2 (IGN). Figure S2 shows the location of the *T*-wave earthquake sources recorded by the DAS arrays.

Figure 9 shows the DAS recordings of the M_w 6.9 Mid-Atlantic Ridge earthquake as recorded by the two DAS arrays. Surface waves are visible both in TF and GC; however, hydroacoustic *T* waves are only recorded in TF. This is because of the hydroacoustic bathymetric blockage by the GC volcanic edifice (see Fig. S2 for the great circle paths between the earthquake

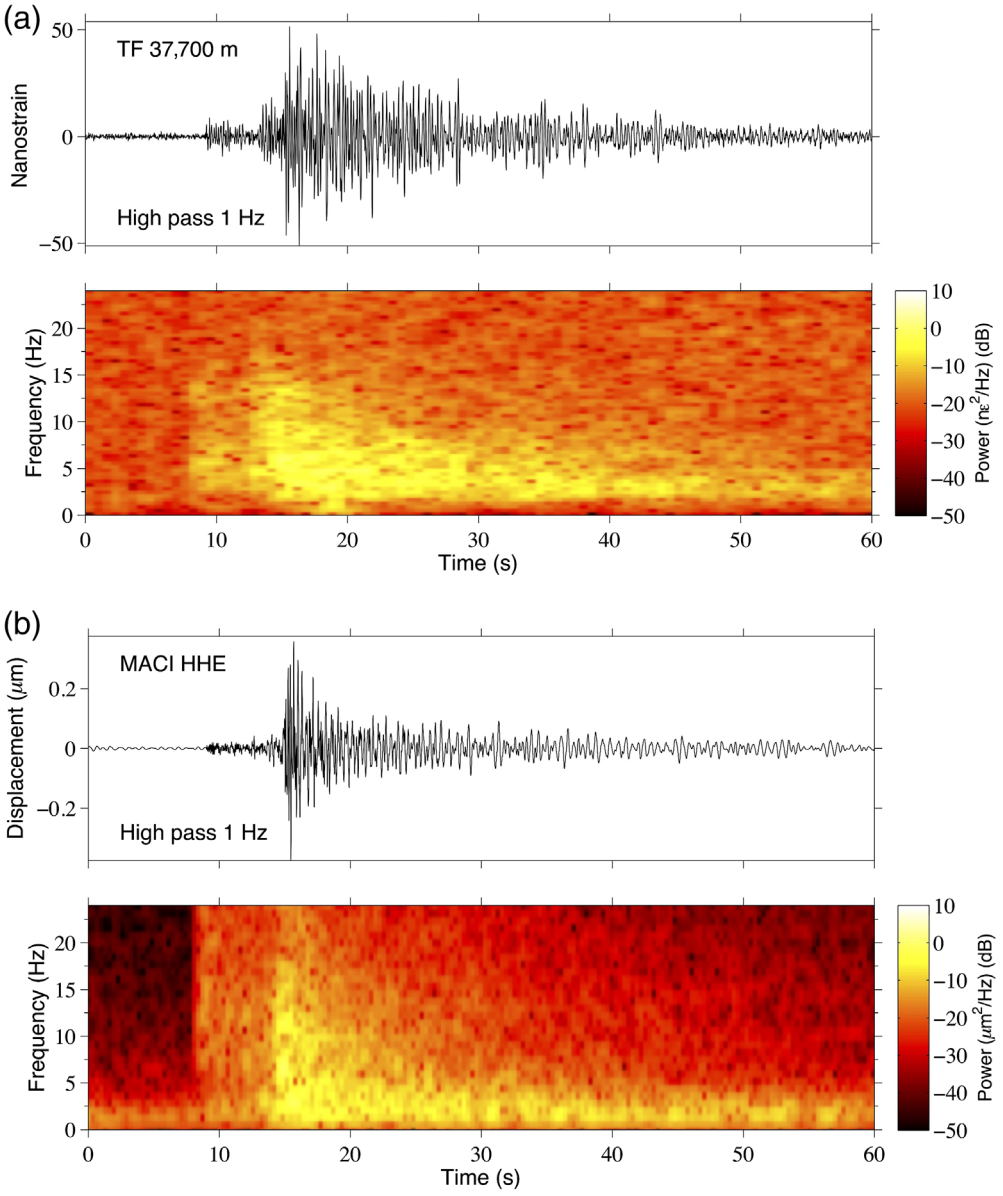

Figure 7. High-pass-filtered observations and spectrogram of the 27 July 2020 m_{bLg} 3.1 earthquake on (a) DAS (fiber position 37.7 km of TF array) and (b) MACI land seismic station (east–west horizontal component). Both data were recorded at about 45 km of epicentral distance, and they are synchronized with respect to the *P*-wave arrival time. The color version of this figure is available only in the electronic edition.

and the two arrays). *T* waves are nonimpulsive signals with long-duration wavetrains of high frequency. Figure 10 shows the raw strain recordings of the hydroacoustic waves for one single channel of the array compared with the seismic *T* waves observed at MACI land seismic station. The *T* waves are recorded with DAS with a high SNR and duration of ~5 min. Strong acoustic energy is observed in the 1–10 Hz range, as derived from the spectral analysis. The *T* waves recorded have strain values greater than those of *P*, *S*, and surface waves (Fig. 8). To determine the propagation velocity from source to receiver, we picked the peak amplitude of the *T*-wave packet envelope; however, the range of observed distances is very small, which does not allow to calculate the apparent velocity through regression (see Fig. S3). This is because the hydroacoustic wavefront is nearly parallel to the TF section of the cable, as it can be observed in Figure S2. Hence, we considered a different approach in which we computed the average velocity from all the arrival times and distances, which gave a more robust estimation of the average data trend. We obtained a velocity value of 1.51 km/s, which is consistent with a propagation path almost entirely in water along the great circle from the epicenter to the fiber. The shape of the *T*-wave package recorded inland, which is very similar to the seafloor DAS recordings, suggests a very efficient acoustic-to-seismic conversion at the steep slopes of TF Island (e.g., Talandier and Okal, 1987). Figure S4 shows another example of *T* waves recorded at GC array.

Discussion

Noise analysis

The strain recordings at the DAS arrays show alternating high and low SNR channel bands persistent over the time duration of the experiment. This observation is especially sharp for the TF array, which presents a higher contrast between noisy and quiet bands than for GC (Figs. 2 and 3). The first high-noise band observed in TF and in GC marks the shoreline crossing of the cable (0 km). The dominant noise in these bands is caused by pressure changes induced by the depth reached by ocean surface waves that affect the recordings up to ~100 m depth (Fig. 3, zoom). The widths of this noise band are 0.8 km in TF and 3.6 km in GC because of the steeper slopes of TF that can be appreciated in the bathymetry map of Figure 1.

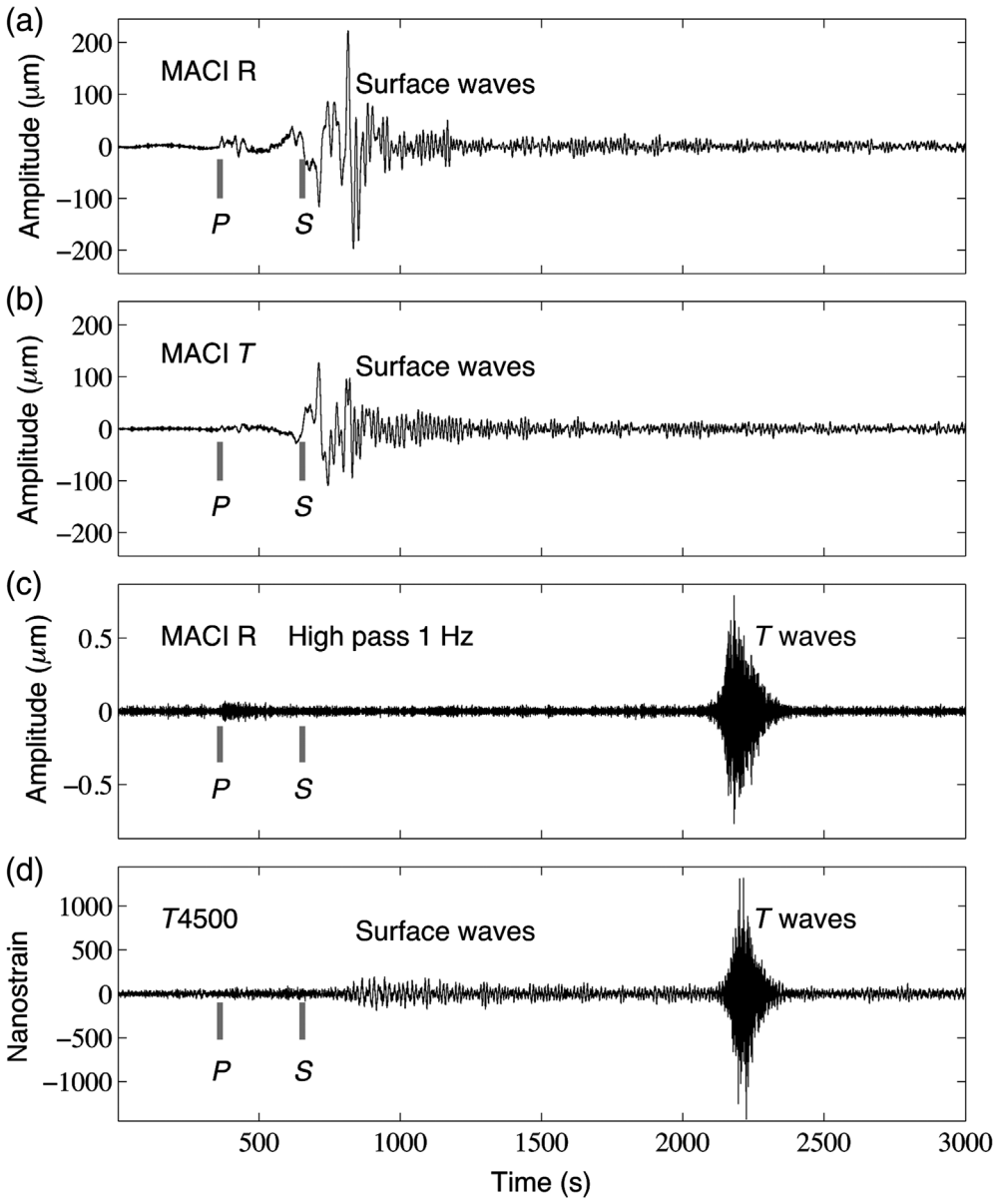

Figure 8. Recordings of the 18 September 2020 M_w 6.9 Mid-Atlantic Ridge earthquake at MACI seismic station: (a) Radial, (b) transversal component, (c) 1 Hz high-pass-filtered radial component, and (d) raw strain recordings (stacked over 100 m). Main *P*, *S*, surface, and hydroacoustic *T* waves are labeled.

The morphology and structure of the submarine region of the volcanic edifices of TF and GC are irregular (Fig. 1), with steep slopes at places, large canyons, slide blocks, and volcanic cones, covered by debris, volcanoclastic, and biogenic sediments (e.g., Ranero *et al.*, 1995; Funck and Schmincke, 1998), which may result in specific local mechanical cable resonances, poor cable coupling, or hanging of the cable in the water column. This can be seen by abrupt changes from high to low SNR sections and existence of strong local resonant frequencies (that also change abruptly) in some sections, as seen in TF between 15 and 20 km (Fig. 3, zoom). For instance, the broad high-noise band observed in GC between 26 and 27 km (Fig. 4) corresponds to an abrupt change in the bathymetry (150 km in Fig. 1b). Instrumental noise (shown to have low variability along the cable in Fig. 2) is not adequate to explain these features also owing to its spatial profile: these "quiet" sections can extend for several kilometers and switch to noisy points (with clear and distinctive acoustic resonances) in a matter of meters.

The DAS recordings in this experiment are not able to detect the primary and secondary microseismic noise peaks in TF, whereas the opposite is true in GC. Observations from other underwater cables (e.g., Sladen *et al.*, 2019; Williams *et al.*, 2019; Matsumoto *et al.*, 2021) showed that primary and especially secondary microseismic activity was visible all along the cable. This difference in TF with previous observations is probably due to several factors, among them the low-strain coupling between cable and ground. In our case, the cable is lying loose on the seafloor, whereas in Williams *et al.* (2019), the cable is buried, and at large water depths. The PSD of the microseisms recorded in Williams *et al.* (2019; reaching [20 dB, 30 dB] rel. to 1 $n\varepsilon^2$/Hz, in the vicinity of 1 Hz) is several orders of magnitude above the acoustic noise floor registered here (reaching [−20 dB, −10 dB] rel. to 1 $n\varepsilon^2$/Hz at 1 Hz, Fig. 2).

Earthquake signals

We also noted that the fiber does not respond equally to the earthquake signals along the array. As it can be observed in Figure 6, no earthquake signal is recorded in TF up to ~1700 m, even for low ambient noise level locations. Lior *et al.* (2021) observed a similar behavior in their dataset and concluded that the lack of earthquake signals in the on-land

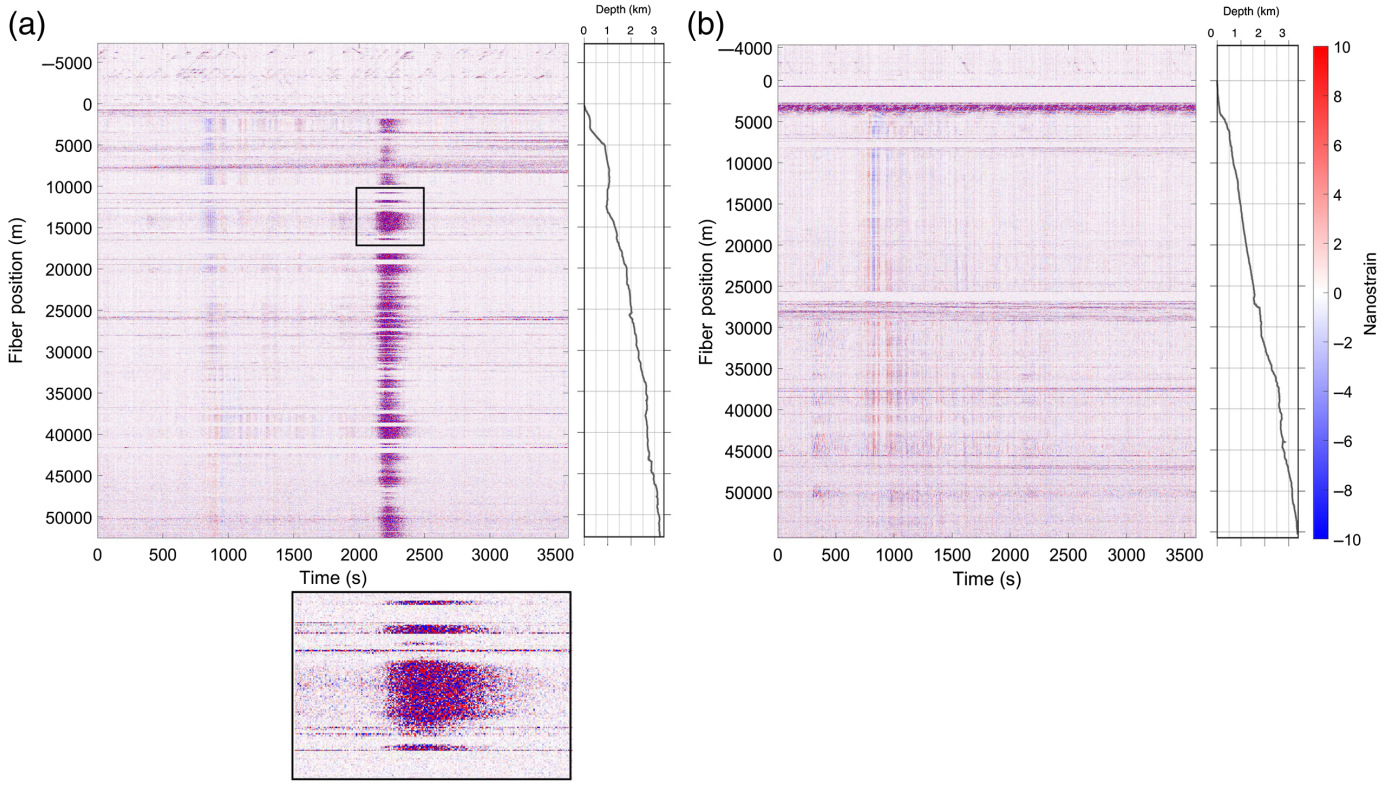

Figure 9. DAS array recordings (time domain, in units of nanostrain) of the 18 September 2020 M_w 6.9 earthquake for the 5984 locations of (a) TF and (b) GC arrays at 10 m spacing. Time is relative to the origin time of the earthquake. The channel depths are also plotted. Space origin (0 km) is relative to shoreline. To enhance visibility of the seismic event, the DAS channel locations, which featured persistent high-noise levels, were substituted with white noise. The zoom-in in the bottom shows that strain energy recorded by the fiber presents high variability from section to section even during high-energy seismic events. The color version of this figure is available only in the electronic edition.

segment of the cable was related to the higher apparent seismic-wave velocities, which causes lower strain recordings as compared with slow velocities. In our case, the lack of seismic signals is observed over the on-land (i.e., [−7.3 km, 0 km]) and shallow underwater ([0 km, 1.7 km]) sections of the cable. Taking into account the uncertainty in the mechanical coupling of the cable on-land and near the shoreline: (1) the cable protection is increased nearing the coast, with double armor in the vicinity of the shoreline, and (2) as the installation conditions on-land change drastically, a high degree of experimental uncertainty is present that deserves further analyses.

The remarkable decrease in local and regional earthquake detection observed in this DAS experiment with respect to the land-based seismic network may be related to different factors. The composition of the submarine cable may provide weak responses or the coupling between the fiber and seafloor sediments (known to have an irregular morphology) may affect the quality of DAS seismic recordings. Another critical factor is the orientation of the fiber-optic cable because this technology only senses in the direction of the fiber. Last but not least, broadband noise levels at the seafloor are high in comparison to land stations (e.g., Frontera *et al.*, 2010), which may increase the detection threshold.

Hydroacoustic *T* waves

The most novel result of this experiment is the identification, for the first time in this type of data, of hydroacoustic *T* waves from oceanic earthquakes at teleseismic and regional distances. The DAS arrays did not detect hydroacoustic waves from earthquakes located in the Central Mid-Atlantic Ridge between latitudes 7.683° and 36.968°N (USGS; see Fig. S2). The reason may be the blockage of the hydroacoustic paths by the islands of the archipelago for sources generated at these latitudes.

Hydroacoustic *T* waves are observed here at abyssal depths up to 3570 m, well below the SOFAR axis depth, which is ~1000 m (Northrop and Colborn, 1974). *T*-phase events have been detected at similar depths in OBS recordings at the southern East Pacific Rise (Shen, 2002) and at depths of 4000–5000 m in French Polynesia (Ito *et al.*, 2012). Butler and Lomnitz (2002) and Butler (2006) explained the detection of *T* phases in the abyssal Pacific Ocean by a coupling mechanism through which seismoacoustic *Ti* waves propagate along

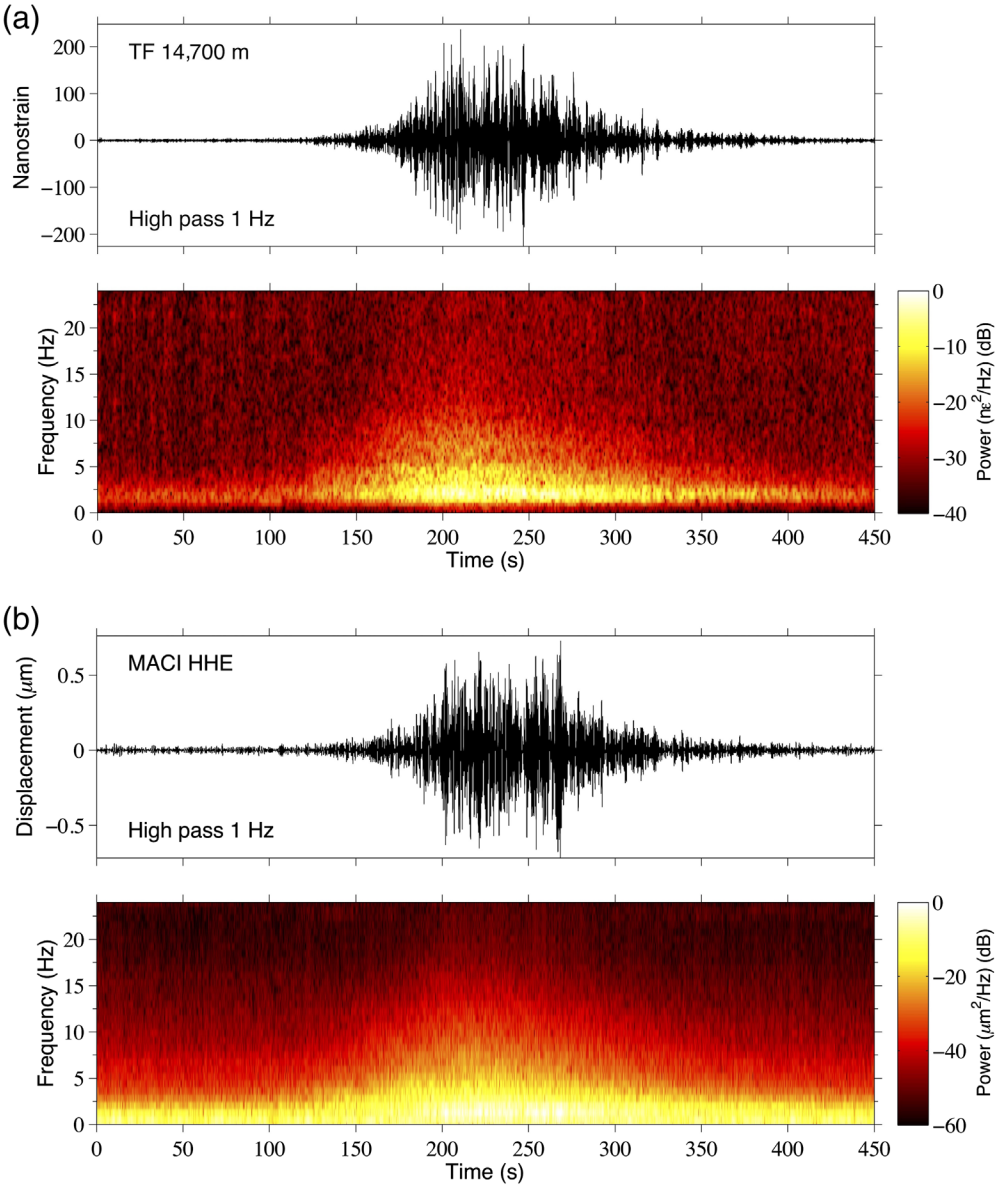

Figure 10. (a) About 1 Hz high-pass-filtered strain recordings and spectrogram of the hydroacoustic waves from the 18 September 2020 M_w 6.9 Mid-Atlantic Ridge earthquake recorded at TF (position 14.7 km). (b) Comparison with the recordings at MACI land station. The color version of this figure is available only in the electronic edition.

the interface between water and sediment at the sound speed of water. Recently, Chen *et al.* (2017) simulated the propagation of *T* waves in deep-ocean basin environments and showed that hydroacoustic energy can propagate effectively from the SOFAR to the abyssal seafloor.

Conclusions

In this study, we analyzed 70 days of DAS strain data recorded along an existing submarine fiber-optic cable in the Canary Islands. Our main findings are as follows:

- Instrumental noise presents a low variability along the cable. The high SNR channels observed persistently, with strong acoustic resonances, may be caused by abrupt bathymetry changes and the installation conditions, with the cable lying loose on the seafloor.
- We confirmed the feasibility of using DAS for underwater seismic detection. The quality of DAS seismic recordings and the detection threshold are affected by the composition and orientation of the submarine cable and the high ambient noise levels at the seafloor.
- In addition to the detection of vehicles along the on-land section of the cable and surface gravity waves, we also verified that DAS is able to detect signals from ships at abyssal depths, which opens the door to explore new applications of this technology in the field of preventive maintenance of submarine cables.
- The experiment revealed signals of hydroacoustic *T* waves, which are clearly visible at depths quite below the SOFAR. *T* waves are valuable for detecting volcanism and earthquake activity in oceanic regions. They are usually recorded by coastal and island-based seismic stations and, more effectively, by OBSs and hydrophone arrays. Here, we demonstrate that the availability of fiber-optic recordings across the oceans can provide inexpensive and powerful detection capabilities for a comprehensive understanding of hydroacoustic energy propagation in remote oceanic regions.

Data and Resources

The Instituto Geográfico Nacional (IGN) catalog is publicly available and was searched through http://www.ign.es/web/ign/portal/sis-

catalogo-terremotos (last accessed February 2021). Some figures of this work were plotted using the Generic Mapping Tools (GMT) software (Wessel *et al.*, 2013). EMODnet Bathymetry Consortium (2020) provided bathymetric data. Supplemental information on the instrument technology and additional figures are compiled as supplemental material.

Declaration of Competing Interests

The authors acknowledge there are no conflicts of interest recorded.

Acknowledgments

The authors are indebted to CANALINK-Canarias submarine link S.L. (http://www.canalink.tel, last accessed February 2021), part of group Instituto Tecnológico y de Energías Renovables (ITER) and Cabildo de Tenerife, for allowing the use of the optical fiber and support during the distributed acoustic sensing (DAS) deployment. The authors gratefully acknowledge RedIRIS (https://www.rediris.es/, last accessed February 2021), particularly Esther Robles and Maribel Cosín, for negotiating the permission for using the submarine link and the accommodation spaces. The authors sincerely thank Editor-in-Chief Allison Bent, Associate Editor Valerie Sahakian, and two anonymous reviewers whose comments and suggestions helped improve and clarify this article. This is a contribution of the Barcelona Center for Subsurface Imaging that is a Grup de Recerca de la Generalitat de Catalunya. With funding from the Spanish government through the "Severo Ochoa Centre of Excellence" accreditation (CEX2019-000928-S), Comunidad de Madrid and Fondo Europeo de Desarrollo Regional (FEDER) Program under Grant SINFOTON2-CM: P2018/NMT-4326, the European Research Council (OCEAN-DAS: ERC-2019-POC-875302), the Spanish Government under projects RTI2018-097957-B-C31, and RTI2018-097957-B-C33. M. R. F.-R. and H. F. M. acknowledge financial support from the Spanish Ministerio de Ciencia e Innovación (MICINN) under Contract Numbers IJC2018-035684-I and IJCI-2017-33856, respectively.

References

Ajo-Franklin, J. B., S. Dou, N. J. Lindsey, I. Monga, C. Tracy, M. Robertson, V. R. Tribaldos, C. Ulrich, B. Freifeld, T. Daley, *et al.* (2019). Distributed acoustic sensing using dark fiber for near-surface characterization and broadband seismic event detection, *Sci. Rep.* **9,** Article Number 1328, doi: 10.1038/s41598-018-36675-8.

Booth, A. D., P. Christoffersen, C. Schoonman, A. Clarke, B. Hubbard, R. Law, S. H. Doyle, T. R. Chudley, and A. Chalari (2020). Distributed acoustic sensing of seismic properties in a borehole drilled on a fast-flowing Greenlandic outlet glacier, *Geophys. Res. Lett.* **47,** e2020GL088148, doi: 10.1029/2020GL088148.

Butler, R. (2006). Observations of polarized seismoacoustic *T* waves at and beneath the seafloor in the abyssal Pacific Ocean, *J. Acoust. Soc. Am.* **120,** 3599–3606, doi: 10.1121/1.2354066.

Butler, R., and C. Lomnitz (2002). Coupled seismoacoustic modes on the seafloor, *Geophys. Res. Lett.* **29,** no. 10, 1418, 57-1–57-4, doi: 10.1029/2002GL014722.

Chen, C.-W., C.-F. Huang, C.-W. Lin, and B.-Y. Kuo (2017). Hydroacoustic ray theory-based modeling of *T* wave propagation in the deep ocean basin offshore eastern Taiwan, *Geophys. Res. Lett.* **44,** 4799–4805, doi: 10.1002/2017GL073516.

Costa, L., H. F. Martins, S. Martin-Lopez, M. R. Fernández-Ruiz, and M. Gonzalez-Herraez (2019). Fully distributed optical fiber strain sensor with $10-12\varepsilon/\sqrt{}$ Hz sensitivity, *J. Lightwave Tech.* **37,** no. 18, 4487–4495, doi: 10.1109/JLT.2019.2904560.

EMODnet Bathymetry Consortium (2020). EMODnet digital bathymetry (DTM), doi: 10.12770/bb6a87dd-e579-4036-abe1-e649cea9881a.

Frontera, T., A. Ugalde, C. Olivera, J. J. Jara, and X. Goula (2010). Seismic ambient noise characterization of a new permanent broadband ocean bottom seismometer site offshore Catalonia (Northeastern Iberian Peninsula), *Seismol. Res. Lett.* **81,** no. 5, 740–749, doi: 10.1785/gssrl.81.5.740.

Fryer, G. J., P. Watts, and L. F. Pratson (2004). Source of the great tsunami of 1 April 1946—A landslide in the upper Aleutian forearc, *Mar. Geol.* **203,** 201–218, doi: 10.1016/S0025-3227(03)00305-0.

Funck, T., and H.-U. Schmincke (1998). Growth and destruction of Gran Canaria deduced from seismic reflection and bathymetric data, *J. Geophys. Res.* **103,** no. B7, 15,393–15,407, doi: 10.1029/98JB00388.

Ito, A., H. Sugioka, D. Suetsugu, H. Shiobara, T. Kanazawa, and Y. Fukao (2012). Detection of small earthquakes along the Pacific-Antarctic Ridge from *T*-waves recorded by abyssal ocean-bottom observatories, *Mar. Geophys. Res.* **33,** 229–238, doi: 10.1007/s11001-012-9158-0.

Lindsey, N. J., and E. R. Martin (2021). Fiber-optic seismology, *Annu. Rev. Earth Planet. Sci.* **49,** 309–336, doi: 10.1146/annurev-earth-072420-065213.

Lindsey, N. J., T. C. Dawe, and J. B. Ajo-Franklin (2019). Illuminating seafloor faults and ocean dynamics with dark fiber distributed acoustic sensing, *Science* **366,** no. 6469, 1103–1107, doi: 10.1126/science.aay5881.

Lindsey, N. J., S. Yuan, A. Lellouch, L. Gualtieri, T. Lecocq, and B. Biondi (2020). City-scale dark fiber DAS measurements of infrastructure use during the COVID-19 pandemic, *Geophys. Res. Lett.* **47,** e2020GL089931, doi: 10.1029/2020GL089931.

Lior, I., A. Sladen, D. Rivet, J.-P. Ampuero, Y. Hello, C. Becerril, H. F. Martins, P. Lamare, C. Jestin, S. Tsagkli, *et al.* (2021). On the detection capabilities of underwater DAS, *J. Geophys. Res.* 126**,** no. 3, e2020JB020925.

Lomax, A., C. Satriano, and M. Vassallo (2012). Automatic picker developments and optimization: FilterPicker—A robust, broadband picker for real-time seismic monitoring and earthquake early-warning, *Seismol. Res. Lett.* **83,** 531–540, doi: 10.1785/gssrl.83.3.531.

Matsumoto, H., E. Araki, T. Kimura, G. Fujie, K. Shiraishi, T. Tonegawa, K. Obana, R. Arai, Y. Kaiho, Y. Nakamura, *et al.* (2021). Detection of hydroacoustic signals on a fiber-optic submarine cable, *Sci. Rep.* **11,** Article Number 2797, doi: 10.1038/s41598-021-82093-8.

McNamara, D., and R. P. Buland (2004). Ambient noise levels in the continental United States, *Bull. Seismol. Soc. Am.* **94,** no. 4, 1517–1527, doi: 10.1785/012003001.

Mezcua, J., E. Buforn, A. Udías, and J. Rueda (1992). Seismotectonics of the Canary Islands, *Tectonophysics* **208,** no. 4, 447–452, doi: 10.1016/0040-1951(92)90440-H.

Northrop, J., and J. G. Colborn (1974). Sofar channel axial sound speed and depth in the Atlantic Ocean, *J. Geophys. Res.* **79,** no. 36, 5633–5641, doi: 10.1029/JC079i036p05633.

Okal, E. A., and J. Talandier (1986). *T*-wave duration, magnitudes and seismic moment of an earthquake: Application to tsunami warning, *J. Phys. Earth* **34,** 19–42, doi: 10.4294/jpe1952.34.19.

Park, M., R. I. Odom, and D. J. Soukup (2001). Modal scattering: A key to understanding oceanic T-waves, *Geophys. Res. Lett.* **28,** 3401–3404, doi: 10.1029/2001GL013472.

Parker, L. M., C. H. Thurber, X. Zeng, P. Li, N. E. Lord, D. Fratta, H. F. Wang, M. C. Robertson, A. M. Thomas, M. S. Karplus, *et al.* (2018). Active-source seismic tomography at the Brady Geothermal Field, Nevada, with dense nodal and fiber-optic seismic arrays, *Seismol. Res. Lett.* **89,** no. 5, 1629–1640, doi: 10.1785/0220180085.

Pastor-Graells, J., J. Nuno, M. R. Fernández-Ruiz, A. Garcia-Ruiz, H. F. Martins, S. Martin-Lopez, and M. Gonzalez-Herraez (2017). Chirped-pulse phase-sensitive reflectometer assisted by first-order Raman amplification, *J. Lightwave Tech.* **35,** no. 21, 4677–4683, doi: 10.1109/JLT.2017.2756558.

Ranero, C. R., M. Torne, and E. Banda (1995). Gravity and multichannel seismic reflection constraints on the lithospheric structure of the canary swell, *Mar. Geophys. Res.* **17,** 519–534, doi: 10.1007/BF01204342.

Rivet, D., B. de Cacqueray, A. Sladen, A. Roques, and G. Calbris (2021). Preliminary assessment of ship detection and trajectory evaluation using distributed acoustic sensing on an optical fiber telecom cable, *J. Acoust. Soc. Am.* **149,** no. 4, 2615–2627, doi: 10.1121/10.0004129.

Rønnekleiv, E., J. K. Brenne, O. H. Waagaard, and B. Moussakhani (2019). Distributed acoustic sensing for submarine cable protection, *SubOptic 2019 Conf.*, New Orleans, Louisiana, USA, 2019, Paper OP4-1.

Shen, Y. (2002). Seismicity at the southern East Pacific Rise from recordings of an ocean bottom seismometer array, *J. Geophys. Res.* **107,** no. B12, EPM 9-1–EPM 9-11, doi: 10.1029/2001JB001742.

Sladen, A., D. Rivet, J. P. Ampuero, L. De Barros, Y. Hello, G. Calbris, and P. Lamare (2019). Distributed sensing of earthquakes and ocean-solid Earth interactions on seafloor telecom cables, *Nat. Comm.* **10,** no. 1, 1–8, doi: 10.1038/s41467-019-13793-z.

Spica, Z. J., K. Nishida, T. Akuhara, F. Pétrélis, M. Shinohara, and T. Yamada (2020). Marine sediment characterized by ocean-bottom fiber-optic seismology, *Geophys. Res. Lett.* **47,** e2020GL088360, doi: 10.1029/2020GL088360.

Talandier, J., and E. A. Okal (1987). Seismic detection of underwater volcanism: The example of French Polynesia, *Pure Appl. Geophys.* **125,** 919–950, doi: 10.1007/BF00879361.

Talandier, J., and E. A. Okal (1998). On the mechanism of conversion of seismic waves to and from *T* waves in the vicinity of island shores, *Bull. Seismol. Soc. Am.* **88,** no. 2, 621–632, doi: 10.1007/BF00879361.

Trabattoni, A., G. Barruol, R. Dreo, A. O. Boudraa, and F. R. Fontaine (2020). Orienting and locating ocean-bottom seismometers from ship noise analysis, *Geophys. J. Int.* **220,** no. 3, 1774–1790, doi: 10.1093/gji/ggz519.

Trautz, R., T. Daley, D. Miller, M. Robertson, G. Koperna Jr., and D. Riestenbergd (2020). Geophysical monitoring using active seismic techniques at the Citronelle Alabama CO_2 storage demonstration site, *Int. J. Greenh. Gas Contr.* **99,** 103084, doi: 10.1016/j.ijggc.2020.103084.

Ugalde, A., B. Gaite, M. Ruiz, A. Villaseñor, and C. R. Ranero (2019). Seismicity and noise recorded by passive seismic monitoring of drilling operations offshore the Eastern Canary Islands, *Seismol. Res. Lett.* **90,** no. 4, 1565–1576, doi: 10.1785/0220180353.

Wessel, P., W. H. F. Smith, R. Scharroo, J. F. Luis, and F. Wobbe (2013). Generic Mapping Tools: Improved version released, *Eos Trans. AGU* **94**, 409–410, doi: 10.1002/2013EO450001.

Williams, E. F., M. R. Fernández-Ruiz, R. Magalhaes, R. Vanthillo, Z. Zhan, M. González-Herráez, and H. F. Martins (2019). Distributed sensing of microseisms and teleseisms with submarine dark fibers, *Nat. Comm.* **10,** no. 5778, doi: 10.1038/s41467-019-13262-7.

Wu, W., Z. Zhan, S. Peng, S. Ni, and J. Callies (2020). Seismic ocean thermometry, *Science* **369,** no. 6510, 1510–1515, doi: 10.1126/science.abb9519.

Yu, C., Z. Zhan, N. J. Lindsey, J. B. Ajo-Franklin, and M. Robertson (2019).The potential of DAS in teleseismic studies: Insights from the Goldstone experiment, *Geophys. Res. Lett.* **46,** 1320–1328, doi: 10.1029/2018GL081195.

Zhan, Z. (2020). Distributed acoustic sensing turns fiber-optic cables into sensitive seismic antennas, *Seismol. Res. Lett.* **91,** no. 1, 1–15, doi: 10.1785/0220190112.

Zhu, T., and D. J. Stensrud (2019). Characterizing thunder-induced ground motions using fiber-optic distributed acoustic sensing array, *J. Geophys. Res.* **124,** 12,810–12,823, doi: 10.1029/2019JD031453.

Zhu, T., J. Shen, and E. Martin (2021). Sensing Earth and environment dynamics by telecommunication fiber-optic sensors: An urban experiment in Pennsylvania, USA, *Solid Earth* **12,** 219–235, doi: 10.5194/se-12-219-2021.

Manuscript received 23 February 2021
Published online 22 September 2021